CHINA FOUNDRY Research & Development
Vol. 23 No. 6 November 2026
www.springer.com/41230
https://doi.org/10.1007/s41230-026-5035-3

Numerical simulation of semi-solid aluminum alloy preparation process by electromagnetic stirring based on dynamic thermophysical parameters

Hao Luo[1], *Xun Zhang[1], Yu Guo[2], Ye Wang[3], Bo Jiang[3], and Jiao-yue Liu[4]

1. School of Architectural Engineering, Harbin University of Science and Technology, Harbin 150040, China

2. School of Intelligent Manufacturing, Huzhou College, Huzhou 313000, Zhejiang, China

3. School of Material Science and Chemical Engineering, Harbin University of Science and Technology, Harbin 150040, China

4. Harbin Boiler Company Limited, Harbin 150040, China

Copyright © 2026 Foundry Journal Agency

Abstract: The electromagnetic stirring method has become one of the important methods for producing semi-solid slurries. Researchers typically use numerical models based on constant thermophysical parameters to predict the desired metrics. However, due to the fact that thermophysical parameters vary with temperature, this model leads to deviations in simulation results. Consequently, in this study, a three-dimensional model based on dynamic thermophysical parameters was constructed to simulate the electromagnetic field-velocity field-temperature field during the electromagnetic stirring of semi-solid aluminum alloy melt. Furthermore, the results were compared with those a constant-parameter model. The simulation model was verified through experiments such as magnetic induction strength measurement, temperature measurement, and metallurgical morphology analysis. The results reveal that the fluctuation trend of velocity at monitoring points obtained from the dynamic thermophysical parameters model exhibits better consistency with the actual situation during three-phase alternating-current electromagnetic stirring. Meanwhile, the temperature distribution trend predicted by the dynamic parameter model aligns more closely with the measured data. In addition, at the monitoring points, the simulated curve based on the dynamic thermophysical parameter model demonstrates superior agreement with the experimental measured values.

Keywords: electromagnetic stirring; semi-solid; aluminum alloy; numerical simulation; dynamic thermophysical parameters

CLC numbers: TP391.9 **Document code:** A **Article ID:** 1672-6421(2026)06-886-15

1 Introduction

The increasing demand for lighter cars and aircraft has led to intensive research into high-strength light metals[1, 2]. Aluminum alloys are extremely important in fields such as transportation engineering and aerospace due to the advantages of energy saving, emission reduction, and automotive lightweighting[3, 4]. Semi-solid forming technology is often used in the manufacture of aluminum alloys to make the microstructure of the alloy more compact and homogeneous, thus allowing the mechanical properties of the alloy to be significantly improved[5]. This molding technique usually applies stirring force to a semi-solid slurry after the alloy slurry is heated to a temperature between the solidus and the liquidus to produce a semi-solid slurry containing near-spherical incipient solid phases[6-8]. During the molding process of the incipient solid phase particles, the grain size can be refined by regulating the stirring intensity and slurry temperature, which in turn enhances the mechanical properties of the material[9, 10]. Since the quality of the alloy slurry determines the quality of the formed alloy component, one of the most critical aspects of semi-solid forming technology is the preparation of alloy semi-solid slurry[11]. To date, researchers have developed various processes for semi-solid slurry preparation[12]. At the

*Xun Zhang

Male, born in 1988, Ph. D., Lecturer. His research interests primarily focus on the numerical simulation of light alloy preparation technology and material design.

E-mail: zhangxun0451@126.com

Received: 2025-02-13; Revised: 2025-10-23; Accepted: 2026-01-20

same time, researchers have experimentally derived suitable slurry preparation process parameters for the indicators such as shape factor and grain size of solid-phase grains[13]. In recent years, the electromagnetic stirring method has become one of the important semi-solid slurry preparation processes[14]. The electromagnetic stirring works by applying an alternating electromagnetic field during the solidification of the slurry using electromagnetic force to stir the melt[15]. This contactless stirring effect can avoid secondary contamination of aluminum alloy slurry[16], and make the solute and temperature distribution of the slurry more uniform, thus reducing the probability of compositional segregation and thermal cracking phenomenon of aluminum alloys[17]. In addition, the process parameters of electromagnetic stirring, such as input frequency, input current, and stirring time[18], are relatively easy to be adjusted and precisely controlled[19]. Therefore, some researchers have also carried out studies on process optimization in electromagnetic stirring based on numerical simulation[20].

For example, Yao et al.[21] investigated the temperature distribution, solute transfer, and solidification behavior during the continuous casting process of round billets by establishing a numerical model of mold electromagnetic stirring. Maurya et al.[22, 23] created different numerical models of electromagnetic stirrers to predict changes in several important indicators by controlling different influencing factors. The magnetic flux density and velocity were analyzed by controlling the width of the electromagnetic stirrer. In addition, by controlling the height of the electromagnetic stirrer, the flow line and liquid phase fraction were analyzed. Kang et al.[24] developed a numerical model for coupled electromagnetic stirring and pulsed current in order to simulate the electromagnetic and flow fields during the solidification of metals under this combined treatment. However, a common limitation in these studies is the use of constant thermophysical parameters in their simulation models. In reality, thermophysical parameters such as density and viscosity vary significantly with temperature, leading to deviations in simulation results.

To address this limitation, some researchers have begun to use dynamic thermophysical parameters in their models. For instance, Guan et al.[25] developed a three-dimensional multiphase solidification numerical model to investigate the effect of combined electromagnetic stirring modes on macroscopic segregation. Huo et al.[26] developed a multi-physics coupled model to investigate the impact of electromagnetic stirring on macroscopic segregation beneath the surface of the billet, with a particular focus on negative segregation. Although their model incorporated some temperature-dependent parameters, a comprehensive comparison with experimental data and an in-depth analysis of the impact of dynamic thermophysical parameters on simulation accuracy ramain insufficient. In this study, a numerical model that utilized dynamic thermophysical parameters, including density and viscosity related to temperature changes, was established to simulate the electromagnetic, velocity, and temperature fields in electromagnetic stirring of semi-solid aluminum alloy melts. The simulation results were then compared with those from a constant parameter model. The simulation model was validated by experiments such as magnetic induction strength measurement, temperature measurement, and metallurgical morphology analysis. The establishment of this model played an important role in improving the macroscopic prediction accuracy of the semi-solid process of aluminum alloy by electromagnetic stirring, thereby facilitating process optimization.

2 Model description

2.1 Coupling model

2.1.1 Basic assumptions

To simplify the calculation while maintaining accuracy, the multiphase flow solidification model is based on the following assumptions[22, 25, 27]:

(1) The model disregards the impact of the melt flow process on the electromagnetic field;

(2) The melt is considered an incompressible Newtonian fluid;

(3) Apart from Joule heat, the electromagnetic model has no internal heat sources;

(4) It is assumed that the magnetic permeability of the aluminum alloy melt during electromagnetic stirring is idential to that of a vaccum.

2.1.2 Governing equations

The basic laws of low-frequency electromagnetic fields were described by Maxwell's differential equations[28]:

$$\nabla\cdot\boldsymbol{B}=0 \tag{1}$$

$$\nabla\cdot\boldsymbol{D}=q_e \tag{2}$$

$$\nabla\times\boldsymbol{E}=-\frac{\partial\boldsymbol{B}}{\partial t} \tag{3}$$

$$\nabla\times\boldsymbol{H}=\frac{\partial\boldsymbol{D}}{\partial t}+\boldsymbol{J} \tag{4}$$

where $\boldsymbol{B}$ is the magnetic induction intensity, $\boldsymbol{D}$ is the electrical induction intensity, q_e is the free charge bulk density, $\boldsymbol{E}$ is the electric field strength, $\boldsymbol{H}$ is the magnetic field strength, and $\boldsymbol{J}$ is the current density at which the induced current is generated by a rotating magnetic field.

Simplified Ohm's law can be used to solve the Maxwell's equations:

$$\boldsymbol{J}=\sigma\boldsymbol{E} \tag{5}$$

$$\boldsymbol{D}=\varepsilon_0\varepsilon_r\boldsymbol{E} \tag{6}$$

$$\boldsymbol{B}=\mu_0\mu_r\boldsymbol{H} \tag{7}$$

where σ is the melt conductivity, ε_0 is the dielectric constant in free space, ε_r is the melt relative permittivity, μ_0 is the magnetic permeability in free space, and μ_r is the melt relative magnetic permeability.

The following equation can be used to represent the electromagnetic force that arises under the action of a rotating magnetic field:

$$\boldsymbol{F}=\boldsymbol{J}\times\boldsymbol{B} \tag{8}$$

The fluid flow model is based on the continuous equations and momentum equations given below:

$$\frac{\partial\rho}{\partial t}+\nabla\cdot\left(\rho\boldsymbol{u}\right)=0 \tag{9}$$

$$\rho\frac{\partial\boldsymbol{u}}{\partial t}+\rho\left(\boldsymbol{u}\cdot\nabla\right)\boldsymbol{u}=-\nabla p+\mu_{\text{eff}}\nabla^2\boldsymbol{u}+\rho\boldsymbol{g}+\boldsymbol{F}+S_{\text{m}} \tag{10}$$

where ρ is the density, $\boldsymbol{u}$ is the velocity vector, p is the pressure, $\boldsymbol{g}$ is the gravitational acceleration, and S_{m} represents the momentum source term generated by the decrease in porosity in the paste zone, as described by Darcy's law:

$$S_{\text{m}}=\frac{(1-\alpha_{\text{m}})^2}{(\alpha_{\text{m}}^3+\xi)}A_{\text{m}}(\boldsymbol{u}-\boldsymbol{u}_{\text{s}}) \tag{11}$$

where α_{m} is the liquid volume fraction, ξ=0.001, A_{m} is the paste zone constant, $\boldsymbol{u}_{\text{s}}$ is the solid phase velocity, and μ_{eff} is the turbulence effective viscosity. The governing equations are solved as follows:

$$\mu_{\text{eff}}=\mu+\mu_{\text{t}}=\mu+\rho C_{\mu}\frac{k^2}{\varepsilon} \tag{12}$$

where μ and μ_{t} are the dynamic viscosity and turbulent dynamic viscosity coefficients of the melt, respectively, C_{μ}=0.0845, k is the turbulent kinetic energy, and ε is the turbulence dissipation rate.

The temperature dependence of the density can be easily adjusted for the alloy melt using linear functions[29-32]:

$$\rho=\rho_{\text{L}}+a(T-T_{\text{L}}) \tag{13}$$

where ρ_{L} is the density at the liquidus temperature, a is the temperature coefficient of the density, and T_{L} is the liquidus temperature.

The dynamic viscosity calculation method uses the Arrhenius equation based on the viscosity-temperature relationship[33-35]:

$$\mu=A\exp\left(\frac{E}{RT}\right) \tag{14}$$

where A is the pre-exponential factor, R is the gas constant, E is the activation energy for viscous flow.

The gas-liquid two-phase interfaces are tracked by solving the volume fraction of the liquid phase, and the liquid phase control equation is as follows[36, 37]:

$$\frac{\partial\alpha_{\text{m}}}{\partial t}+\boldsymbol{u}\cdot\nabla\alpha_{\text{m}}=0 \tag{15}$$

In the calculation of physical properties such as density and viscosity, these parameters are primarily defined as a function of the volume fraction of the liquid phase. This relationship can be mathematically represented as follows:

$$\rho=\alpha_{\text{m}}\rho_{\text{l}}+(1-\alpha_{\text{m}})\rho_{\text{g}} \tag{16}$$

$$\mu=\alpha_{\text{m}}\mu_{\text{l}}+(1-\alpha_{\text{m}})\mu_{\text{g}} \tag{17}$$

where ρ_{l} is the liquid phase density, ρ_{g} is the gas phase density, μ_{l} is the liquid phase viscosity, and μ_{g} is the gas phase viscosity.

The following equations are used to solve the turbulent kinetic energy and turbulent dissipation rate based on the Navier-Stokes equation:

$$\rho\frac{\text{d}k}{\text{d}t}=\nabla\cdot[(\alpha_k\mu_{\text{eff}})\nabla k]+G_k+G_b-\rho\varepsilon \tag{18}$$

$$\rho\frac{\text{d}\varepsilon}{\text{d}t}=\nabla\cdot[(\alpha_k\mu_{\text{eff}})\nabla\varepsilon]+C_{1\varepsilon}\frac{\varepsilon}{k}(G_k+C_{3\varepsilon}G_b)-C_{2\varepsilon}\rho\frac{\varepsilon^2}{k} \tag{19}$$

where G_k represents the generation of turbulent kinetic energy due to the average velocity gradient, G_{b} represents the generation of turbulent kinetic energy due to buoyancy effects, $G_{1\varepsilon}$, $G_{2\varepsilon}$, and $G_{3\varepsilon}$ are empirical constants, α_k and α_{ε} are the reciprocal of the effective turbulent Prandtl numbers for turbulent kinetic energy and turbulent dissipation rate, respectively.

The heat exchange between the inner and outer regions of the alloy melt during solidification can be expressed using the energy conservation equation:

$$\rho C_{\text{p}}\frac{\partial T}{\partial t}+\rho C_{\text{p}}(\boldsymbol{u}\cdot\nabla)T=\lambda\nabla^2T+Q_{\text{L}}+Q_{\text{J}} \tag{20}$$

where T is the temperature, C_{p} is the specific heat capacity of the melt, Q_{L} is the solidification latent heat of the alloy during solidification, λ is the melt thermal conductivity. The dynamic thermal conductivity of the melt is calculated using a semi-empirical equation based on the relationship between thermal conductivity and temperature[38, 39]:

$$\lambda=\lambda_0+b(T-T_{\text{L}}) \tag{21}$$

where λ_0 is the thermal conductivity at the melting point, b is the temperature coefficient of the thermal conductivity. Q_{J} is the Joule heat from induced current, calculated as follows:

$$Q_{\text{J}}=\int J\cdot E\text{d}V \tag{22}$$

Table 1 lists the values of a, E, and λ_0.

Table 1: Key parameters for partial modeling

Parameters	Value
Temperature coefficient of the density, a [kg·(m^3·K)$^{-1}$]	−0.0006[30]
Activation energy for viscous flow, E (J·mol^{-1})	1.4×10^5[40]
Thermal conductivity at the melting point, λ_0 [W·(m·K)$^{-1}$]	110[41]

2.2 Geometric model

The schematic diagram of the electromagnetic stirrer models is shown in Fig. 1. The model was simplified to an electromagnetic stirrer with six coil windings near the iron core while ensuring accuracy. The outer diameter of the iron core was 580 mm and the inner diameter was 350 mm. Each coil winding had 104 turns. Three-phase alternating current was applied to the coil winding and the low-frequency current from the power source created a rotating magnetic field. The electromagnetic stirrer was used to stir A356 aluminum alloy melt with a height of 100 mm in a crucible. The thickness of the crucible was 10 mm, and the inner cavity size was Φ80 mm×120 mm.

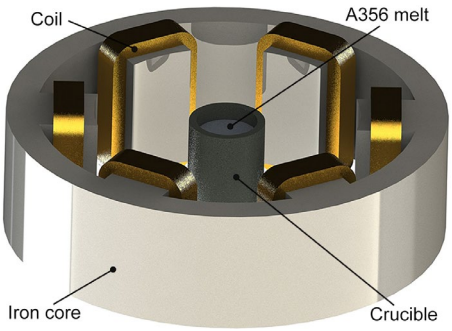


Fig. 1: Schematic diagram of electromagnetic stirrer models

2.3 Boundary conditions

2.3.1 Electromagnetic model

The boundary conditions that are relevant to the electromagnetic simulation model are as follows:

(1) The electromagnetic stirrer was composed of three pairs of coil windings, which applied three-phase alternating current to generate a rotating magnetic field;

(2) The iron core and coil winding of the electromagnetic stirrer were set with insulation boundary conditions;

(3) The magnetic flux lines on the outer surface of the air unit around the electromagnetic stirrer were parallel to the boundary of the air domain;

(4) The magnetic potential of the outermost component of the electromagnetic stirrer was zero.

2.3.2 Velocity and temperature field model

The boundary conditions that are relevant to the velocity and temperature simulation model are as follows:

(1) Top surface: For heat exchange between the melt and the outside, vents were set and the normal gradient was set to 0 for all variables;

(2) Wall surface: Convective heat transfer took place between the melt and the inner wall of a graphite crucible. Due to the asbestos insulating layer on the outside of the crucible, an external heat transfer condition of 853 K occured on the outer wall. The stress component perpendicular to the wall contact surface was assumed to be 0.

2.4 Solution procedure

In this study, the numerical simulation was carried out using the software ANSYS, and three-phase alternating electromagnetic field data were calculated based on Maxwell equations. In addition to loading electromagnetic fields by magnetohydrodynamics (MHD) modules, the user-defined function (UDF) of physical parameters related to dynamic thermal changes was required to be written into the numerical model. A transient simulation was performed using the pressure-based SIMPLE algorithm with a time step of 0.002 s until the specified time. Table 2 lists the parameters involved in the numerical model.

2.5 Experimental process

Figure 2 shows the process of preparing A356 alloy by electromagnetic stirring. Initially, a crucible with A356 aluminum alloy was placed and heated in a melting furnace. After the aluminum alloy was completely melted, the crucible was transferred to an electromagnetic stirrer. Electromagnetic stirring was started after completing the adjustment of the electromagnetic stirrer system and industrial chiller. During the electromagnetic stirring process, the temperature and magnetic induction intensity were monitored by thermocouples and Gaussmeters, respectively. After electromagnetic stirring was

Table 2: Parameters and material properties in simulation[42]

Parameters	Value
Solidus temperature of the melt (K)	828
Liquidus temperature of the melt (K)	888
Latent heat of the melt ($J \cdot kg^{-1}$)	3.98×10^5
Specific heat capacity of the melt [$J \cdot (kg \cdot K)^{-1}$]	963
Input current (A)	100
Input frequency (Hz)	5, 10, 15
Electrical conductivity of the melt ($S \cdot m^{-1}$)	2.451×10^7
Magnetic permeability of the melt ($H \cdot m^{-1}$)	1.257×10^{-6}

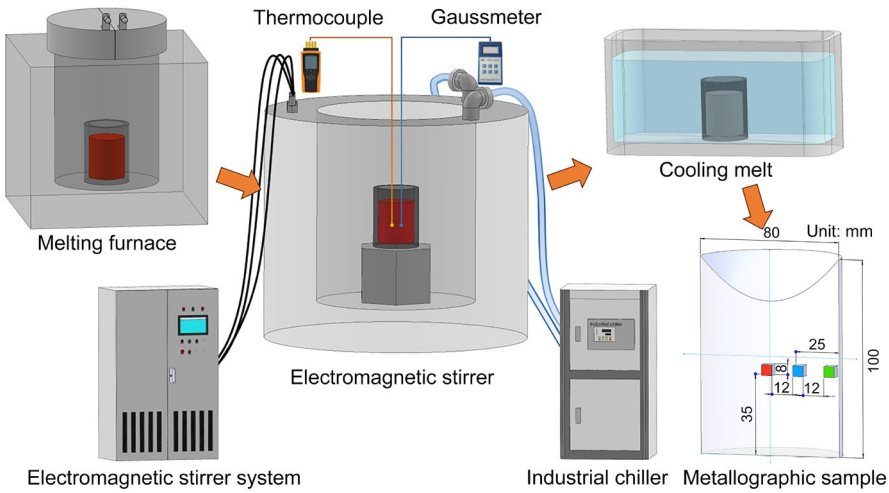


Fig. 2: Schematic diagram for the fabrication of A356 alloy by electromagnetic stirring

completed, the crucible was placed in a cooling bath for water quenching. The cooled finished ingot was then removed from the crucible. Using a wire cutter, 8 mm cubes were cut out from the specified positions of the ingot. The samples were then sanded and polished. Finally, after chemical etching with 0.5% hydrofluoric acid solution, the surface of the finished sample was observed with a metallographic microscope. Statistical results of average grain size were completed using software ImageJ.

3 Results and discussion

3.1 Magnetic induction intensity distribution

Electromagnetic forces are the driving force of melt flow. The simulation of the electromagnetic field is essential for modeling the electromagnetic stirring process, serving as the foundation for subsequent velocity and temperature fields calculations. Since no temperature-dependent dynamic parameters are involved in the simulation of the electromagnetic field, both constant and dynamic thermophysical parameter models can be modeled with the same calculation results for electromagnetic fields.

During the electromagnetic stirring process, the electromagnetic frequency has a major influence on the stirring effect. When the current is 100 A and the input frequencies are 5 Hz, 10 Hz, and 15 Hz, the distribution of magnetic induction intensity is shown in Fig. 3. It is obvious from the graph that as the frequency increases, the red region near the wall gradually decreases. Meanwhile, the coverage of the blue region in the core gradually increases, indicating that the penetration depth of the magnetic field gradually decreases.

Figure 4 shows the radial magnetic induction intensity distribution of the melt cross section at different frequencies. The numerical value of magnetic induction intensity shows a trend of low center and high edge, and this trend gradually becomes apparent with the increase of frequency. The magnetic induction intensity at the designated location was measured through verification experiments. The trend measured in the experiment basically agrees with that calculated in the simulation.

3.2 Distribution of density and viscosity

During the simulation process, the density and viscosity in the thermophysical parameters are significantly affected by temperature. Therefore, in this section, the density and viscosity distributions in the dynamic and constant thermophysical parameter models at different frequencies and stirring times are compared.

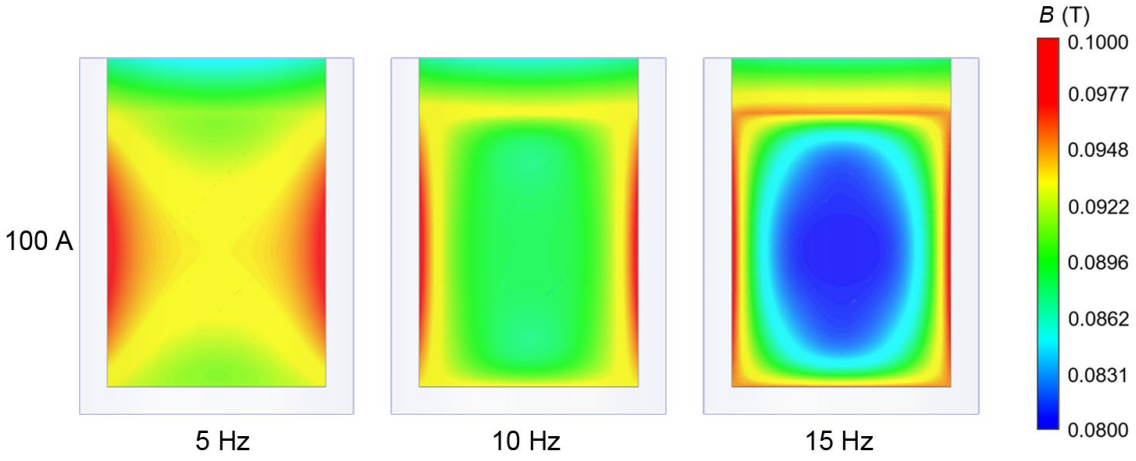


Fig. 3: Distribution of magnetic induction intensity in melt at different frequencies with an input current of 100 A

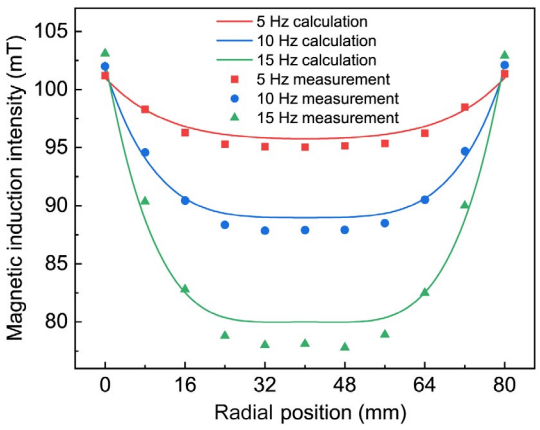


Fig. 4: Distribution of magnetic induction intensity along the radial direction of the melt with an input current of 100 A

3.2.1 Distribution of density and viscosity at different frequencies

Figure 5 shows the distribution of thermophysical parameters at different frequencies, with the stirring time and input current fixed at 45 s and 100 A, respectively. For clarity, the blue region represents air, the red region denotes the melt, and the green and yellow regions correspond to the interface between air and the melt. Figure 5(a) shows the distribution of thermophysical parameters for the constant parameter model. It can be seen that the density and viscosity of air and the melt exhibit significant differences. As the input frequency increases, the fluctuation amplitude of the liquid level increases. However, the thickness of the gas-liquid mixing zone is consistent at the center and edge, which is almost unaffected by frequency. The melt density and viscosity of the model with constant thermophysical

parameters are 2,681.86 kg·m^{-3} and 2.520×10^{-5} kg·(m·s)$^{-1}$, respectively. The density and viscosity of air are 1.225 kg·m^{-3} and 1.789×10^{-5} kg·(m·s)$^{-1}$, respectively. The thermal physical parameter distribution of the dynamic parameter model at different frequencies is shown in Fig. 5(b). It can be seen that as the frequency increases, the amplitude of the liquid level fluctuations increases and due to the influence of dynamic thermophysical parameters, the fluctuation amplitude of liquid level increases with the increase of frequency. Different from the results of the constant parameter model, the distribution of gas-liquid mixing is wide in the center and narrow in the edge.

In order to investigate the variation trend of thermal physical parameters in dynamic parameter models, the density and viscosity distribution along the radial direction of the melt center were analyzed. When the stirring time and input current are 45 s and 100 A respectively, the distribution of dynamic thermophysical parameters along the radial direction in melt center at different input frequencies is shown in Fig. 6. It can be seen that the distribution trends of density and viscosity are approximately the same. As the frequency increases, the density and viscosity gradually decrease near the wall, while an opposite trend is observed in the middle. At a distance of 8 mm from the wall, the change trend turns and the values at each frequency are close. It indicates that changes in input frequency have minimal impact on the density and viscosity in this region. Meanwhile, when the input frequencies are 10 Hz and 15 Hz, respectively, the difference in the distribution curves of the density and viscosity parameters is minimal. This means that when the frequency reaches 10 Hz, increasing the input frequency has little effect on density and viscosity.

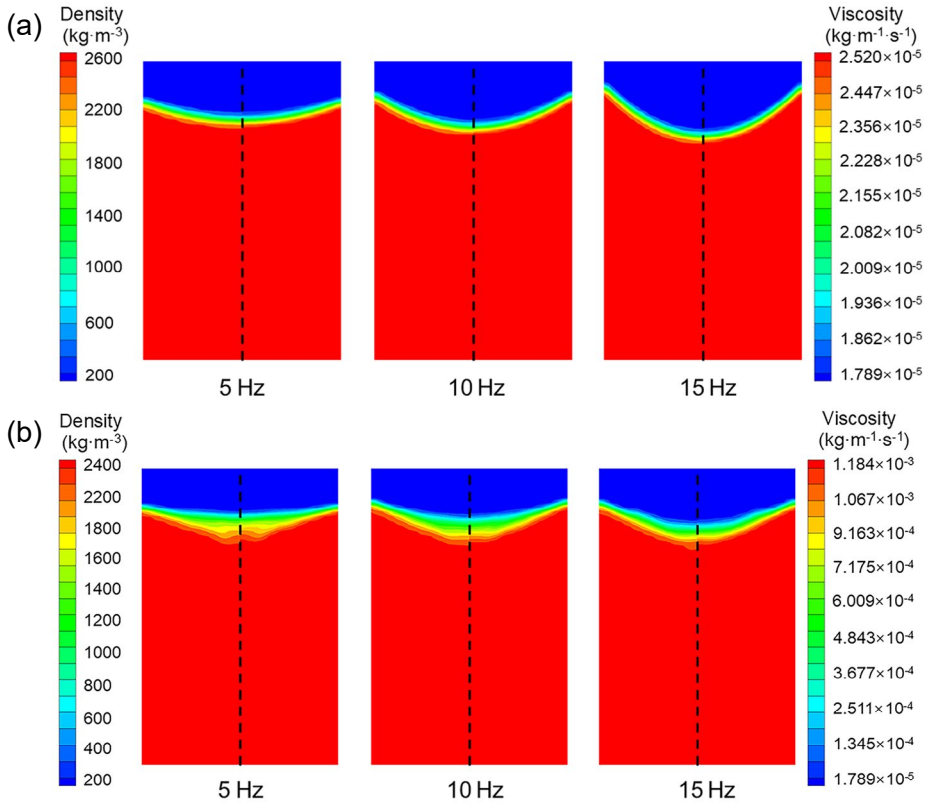


Fig. 5: Thermophysical parameter distribution at 45 s for different frequencies with an input current of 100 A: (a) constant thermophysical parameters; (b) dynamic thermophysical parameters

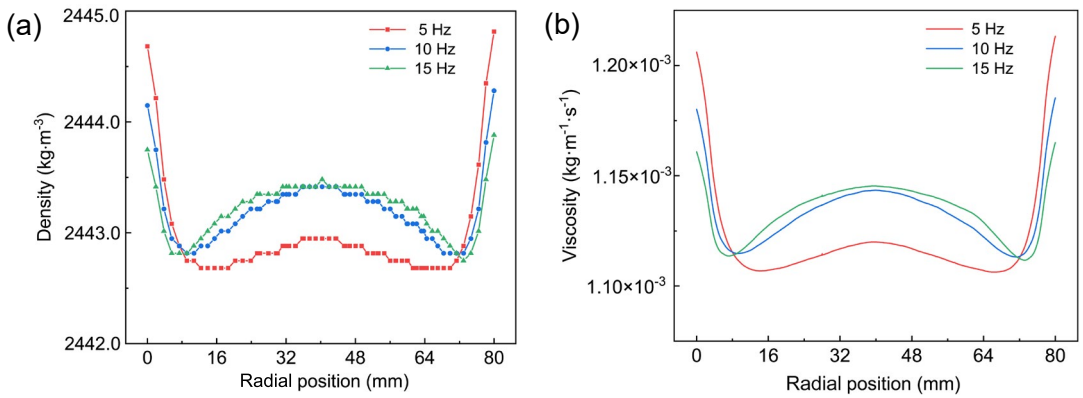


Fig. 6: Distribution of dynamic thermophysical parameters along the radial direction at 45 s for different frequencies with an input current of 100 A: (a) density; (b) viscosity

3.2.2 Distribution of density and viscosity at different times

The thermal physical parameter distribution at different times with an input frequency of 15 Hz and an input current of 100 A is shown in Fig. 7. Figure 7(a) shows the thermal physical parameter distribution of the constant parameter model. It can be seen that as time increases, the amplitude of liquid level fluctuations gradually increases and tends to be stable after 45 s. Under constant parameters, the thickness of the gas-liquid mixing zone is almost unaffected by an increase in time. Figure 7(b) shows the thermal physical parameter distribution of the dynamic parameter model at different times. The amplitude of liquid level fluctuations decreases with time, and the gas-liquid mixing zone gradually expands to a certain extent due to the influence of changing thermophysical parameters.

In order to investigate the influence of the stirring time on the trend of thermal physical parameter changes, the density and viscosity distribution along the radial direction of the melt were analyzed. When the input frequency and input current are 15 Hz and 100 A, respectively, the distribution of dynamic thermophysical parameters along the center diameter of the melt at different stirring times is shown in Fig. 8. Between 30 s and 45 s of stirring time, it can be observed that the density and viscosity almost do not change near the wall. As time progresses, the lowest density and viscosity values gradually shift from the middle position to both sides simultaneously, and this trend begins to weaken after 45 s. It can be seen from Fig. 8 that as time goes on, the viscosity and density gradually increase overall. Due to the increase in viscosity and density, the trend of liquid level fluctuations gradually becomes smoother.

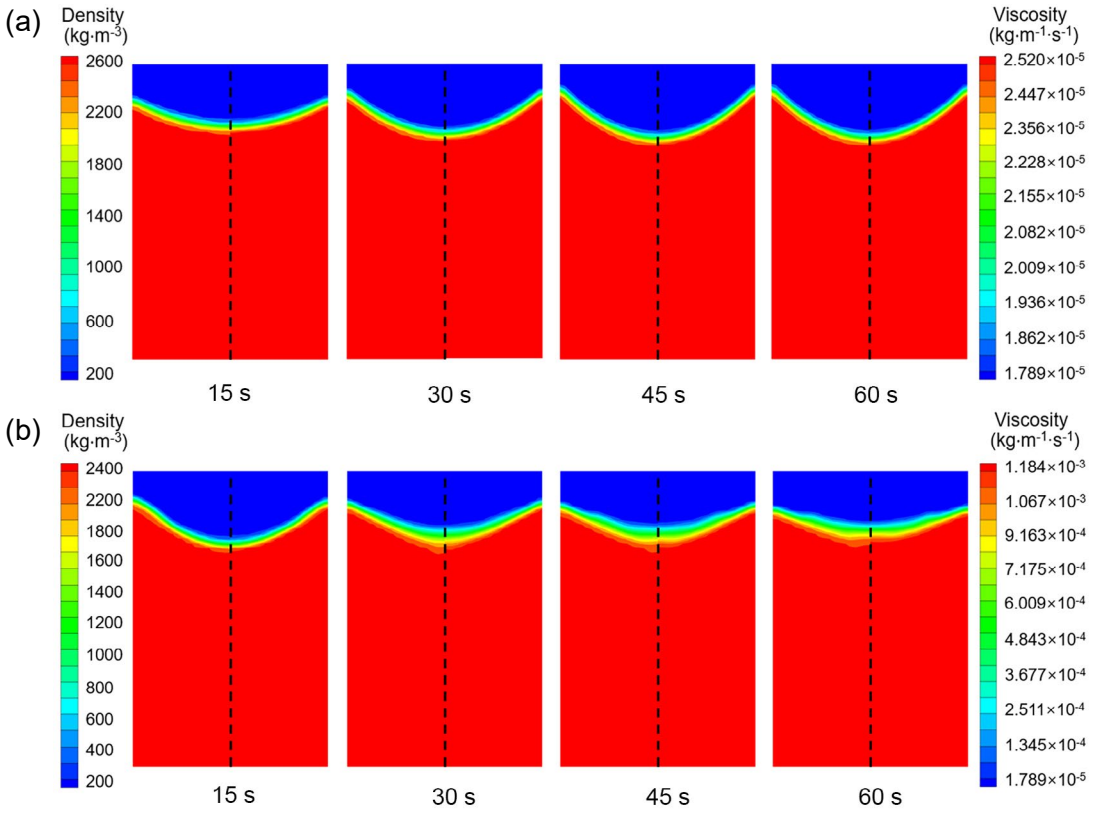


Fig. 7: Thermophysical parameter distribution at different times with an input frequency of 15 Hz and an input current of 100 A: (a) constant thermophysical parameters; (b) dynamic thermophysical parameters

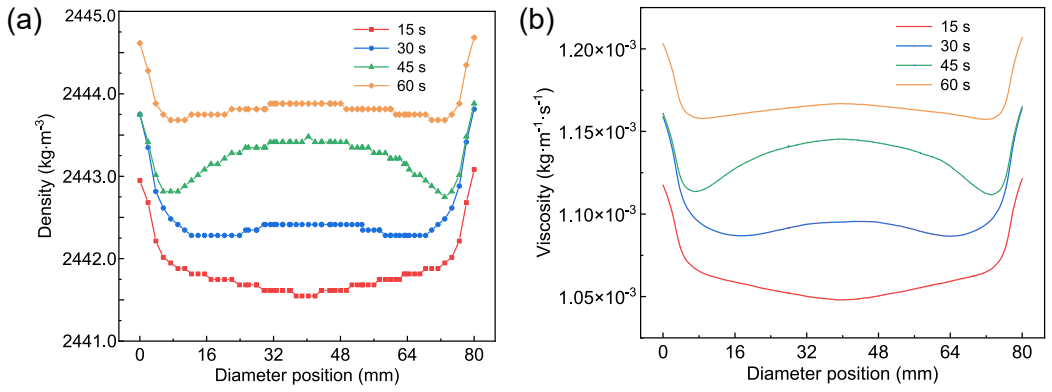


Fig. 8: Distribution of dynamic thermophysical parameters along the radial direction in melt center at different times with an input frequency of 15 Hz and an input current of 100 A: (a) density; (b) viscosity

3.3 Velocity distribution

3.3.1 Velocity distribution at different frequencies

Figure 9 shows the velocity distribution at different frequencies when the input current is 100 A and the stirring time is 45 s. Figure 9(a) shows the velocity distribution of constant thermophysical parameters model. As the input frequency increases, the velocity near the wall increases significantly. Meanwhile, the velocity of the melt in the center is almost zero, and the velocity band is vertically distributed. The velocity distribution of dynamic thermophysical parameters model at different frequencies is shown in Fig. 9(b). It is obvious that the velocity distribution of the model with dynamic thermophysical parameters is different from that of the model with constant parameters. As the frequency increases, the velocity of the entire melt shows an upward trend. The high velocity region shows a crescent-symmetrical distribution in the vertical cross-section due to the changing viscosity near the wall side. At the same time, even if the viscosity change in the central region is not obvious, it is evident from Fig. 9(b) that the coverage area of the blue region, which represents a low velocity, gradually shrinks with increasing frequencies, which can be clearly seen on the surface and bottom of the melt.

3.3.2 Velocity distribution at different times

The velocity distribution at different stirring times with an input frequency of 15 Hz and an input current of 100 A is shown in Fig. 10. Figures 10(a) and (b) show the velocity distribution of constant and dynamic thermophysical parameters models, respectively. The coverage area of the red region over time, which represents high velocity, expands inward under the constant thermophysical parameters model. Meanwhile, the degree of fluctuation of the liquid level is gradually increasing. The velocity field with dynamic thermophysical parameters exhibits significant differences from that with constant thermophysical parameters. This is because parameters in the dynamic thermophysical parameter model change over time, for instance, the viscosity coefficient increases with time, which in turn leads to a reduction in the high-velocity region, significant fluctuations in the gas-liquid interface velocity, and an expansion of the low-velocity region.

Figure 11 shows the variation of melt velocity with time at the radial position of 30 mm and the axial height of 50 mm. When using constant thermophysical parameters, the velocity of the monitoring point increases to about 0.486 $m \cdot s^{-1}$ in a short time and stabilizes at approximately 0.48 $m \cdot s^{-1}$. When using dynamic thermophysical parameters, the velocity of the monitoring points also increases to a certain value in a short time. Subsequently, the velocity shows fluctuations over time, with an overall slight decreasing trend. The electromagnetic model in this study uses three-phase alternating current, and the electromagnetic force undergoes periodic changes within the coverage area of the magnetic field. Obviously, simulation models using dynamic thermophysical parameters are relatively more accurate.

3.4 Temperature distribution and particles motion

3.4.1 Temperature distribution at different frequencies

Due to the fact that the thermophysical parameters of the dynamic parameter model are controlled by temperatures, it is necessary to analyze the temperature changes. This section examines the influence of different frequencies on temperature changes by controlling the input frequency.

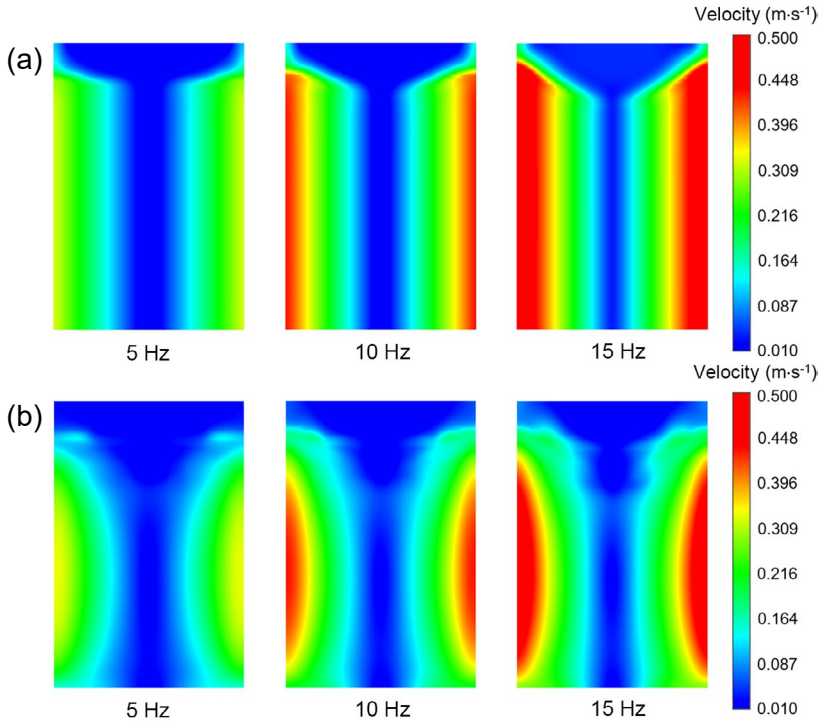


Fig. 9: Velocity distribution at different frequencies when the input current is 100 A and the stirring time is 45 s: (a) constant thermophysical parameters; (b) dynamic thermophysical parameters

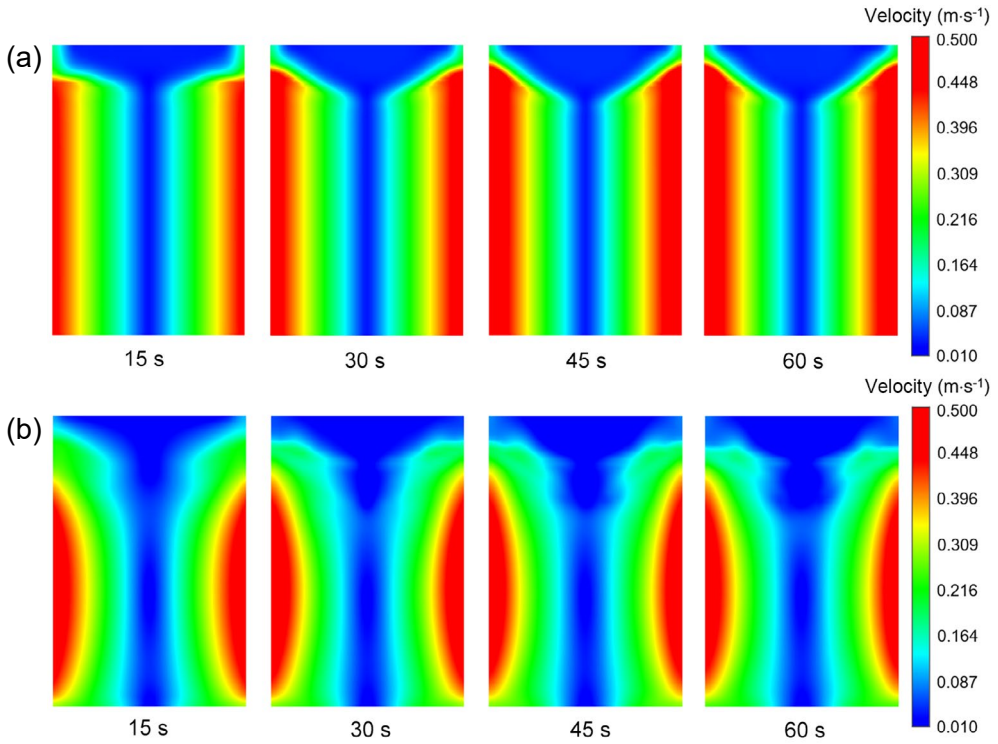


Fig. 10: Velocity distribution at different times with an input frequency of 15 Hz and an input current of 100 A: (a) constant thermophysical parameters; (b) dynamic thermophysical parameters

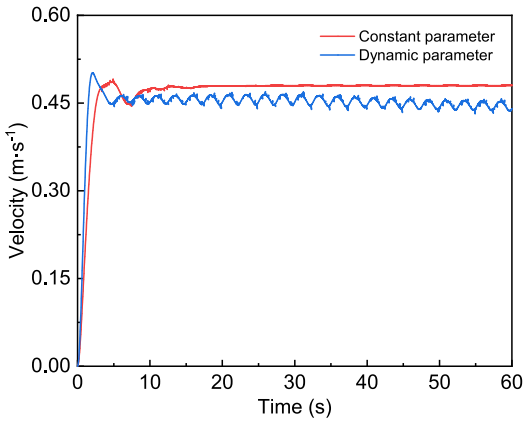


Fig. 11: Change in velocity over time at the radial position of 30 mm and axial height of 50 mm

When the stirring time and input current are 45 s and 100 A, respectively, the temperature distribution of the constant parameter model under different frequencies and without electromagnetic stirring is shown in Fig. 12. It can be seen that the temperature distribution trend with electromagnetic stirring is similar to that without electromagnetic stirring. This phenomenon means that the magnetic field has little influence on the temperature distribution when using a model with constant thermophysical parameters. As the input frequency increases, the extent of the internal high-temperature region gradually shrinks, while the temperature distribution in the upper part of the melt becomes arcuate, with its curvature progressively increasing.

Figure 13 shows the temperature distribution of the dynamic parameter model without electromagnetic stirring under different frequencies when the stirring time and input current are 45 s and 100 A, respectively. It can be seen that without electromagnetic stirring, the trend of temperature distribution is basically consistent using dynamic and constant thermophysical parameters, starting from the outside to the inside for heat dissipation. When electromagnetic stirring is applied to the melt, the trend of temperature distribution is significantly different from that without electromagnetic stirring. It is evident that the velocity field produced by the model with dynamic thermophysical parameters under electromagnetic stirring causes the lower melt region to dissipate heat from the inside out. As the input frequency increases, the low-temperature region in the lower part of the melt expands, while the upper low-temperature region generated by heat exchange with air, expands downward. The overall temperature of the melt decreases with increasing frequency.

When the stirring time and input current are 45 s and 100 A, respectively, the distribution of the calculated temperature and the measured temperature along the radial direction of the melt at different input frequencies is shown in Fig. 14. The calculated temperature in Fig. 14(a) is based on a constant thermophysical parameter model, while that in Fig. 14(b) is based on a dynamic thermophysical parameter model. The temperature difference between the constant parameter model and the experimentally measured temperature is 3–5 K, while the temperature difference between the dynamic parameter model and the experimentally measured temperature is 1–3 K. The temperature distribution trend of the dynamic parameter model is closer to the distribution trend of the measured temperature. Obviously, dynamic thermophysical parameter models are relatively more accurate.

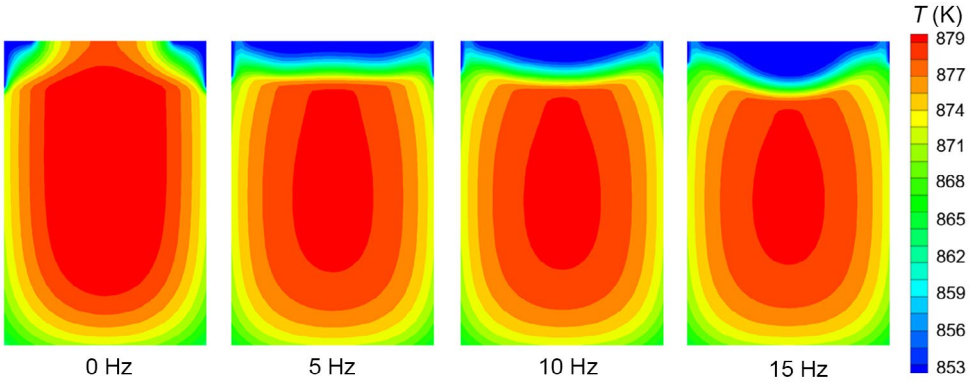


Fig. 12: Temperature distribution of constant parameter models at 45 s for different frequencies with an input current of 100 A

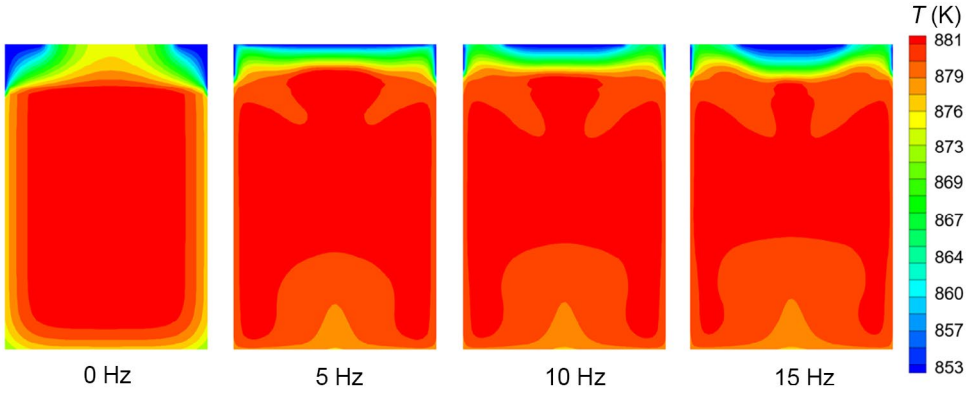


Fig. 13: Temperature distribution of dynamic parameter models at 45 s for different frequencies with an input current of 100 A

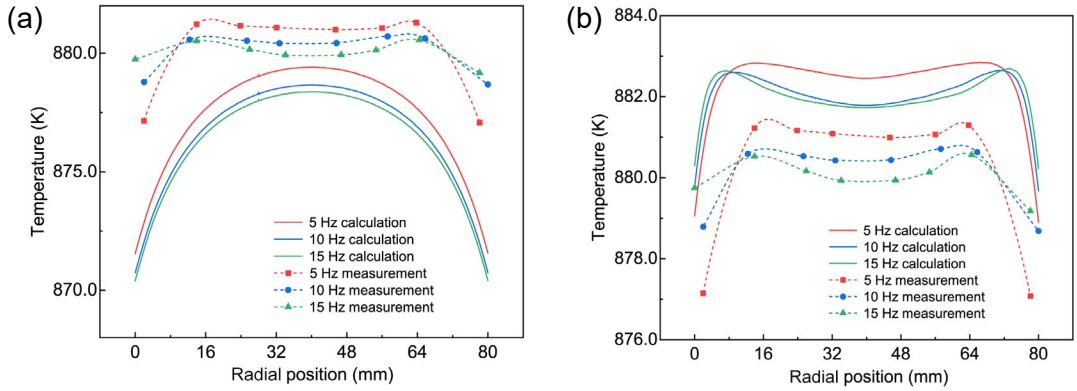


Fig. 14: Temperature distribution along the radial direction at 45 s for different frequencies with an input current of 100 A: (a) constant parameter models; (b) dynamic parameter models

In addition to using a Gaussian meter to check the magnetic field and a thermocouple to check the temperature field, analyzing the metallography of the alloy after water quenching can also verify the accuracy of the distribution trend of the simulation model results. The metallographic diagrams at different positions of the central cross-section of the sample at 100 A and different frequencies are shown in Fig. 15. In order to visualize the metallographic changes of different process parameters, as shown in Fig. 16, statistical analysis was conducted on the average grain size at different positions based on the metallographic micrograph. At input frequencies of 5 Hz and 10 Hz, a pronounced disparity in the average grain size emerges between the center and edge of the sample. Obviously, at an input frequency of 15 Hz, due to the average grain size of the samples measured at different positions are close to each other, the average radial temperature difference is the smallest, which is more consistent with the prediction of temperature distribution by the dynamic thermophysical parameter model.

3.4.2 Temperature distribution at different times

During the electromagnetic stirring process, the temperature inside the melt changes significantly with the stirring time. In this section, the temperature distribution at different stirring times is analyzed to investigate the differences between constant and dynamic thermophysical parameter models.

The temperature distribution using constant thermophysical

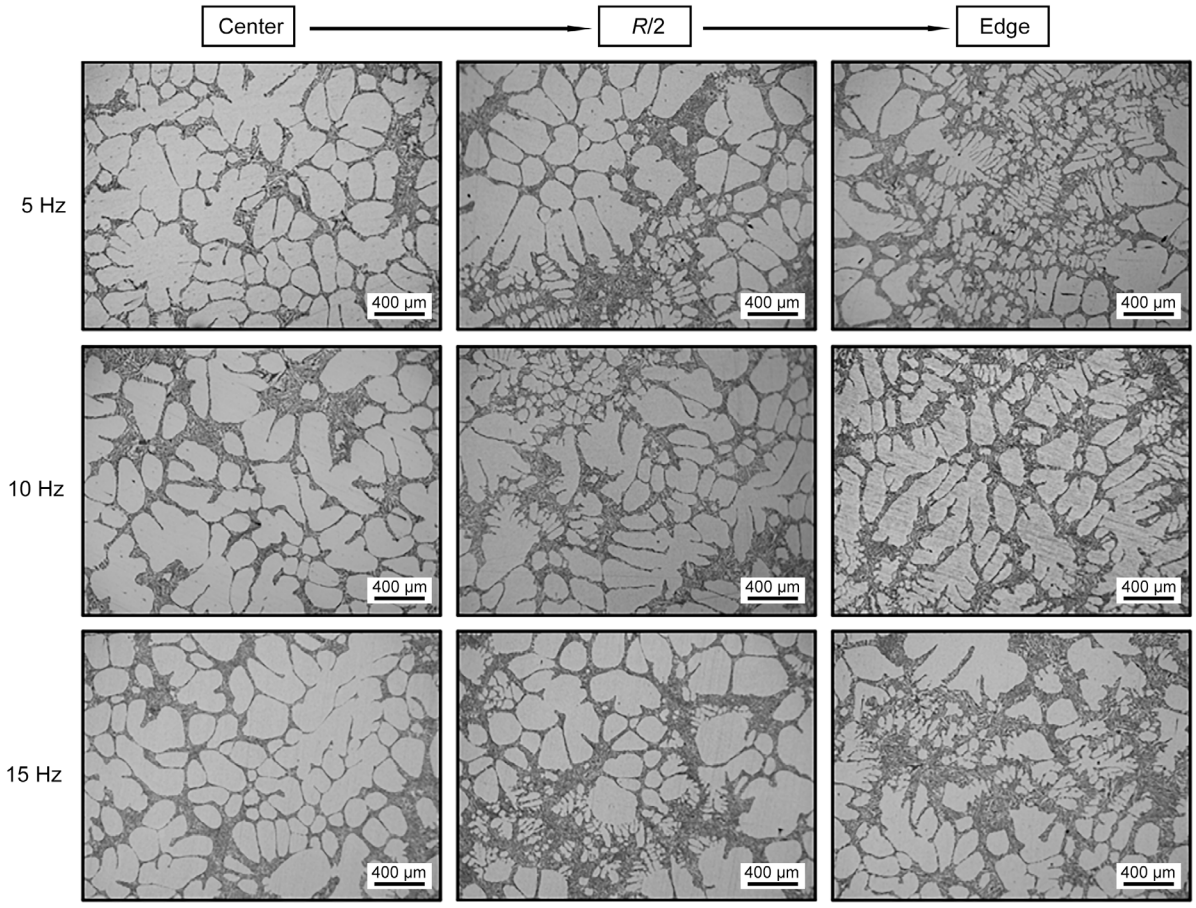


Fig. 15: Metallographic diagrams of samples at different frequencies with an input current of 100 A

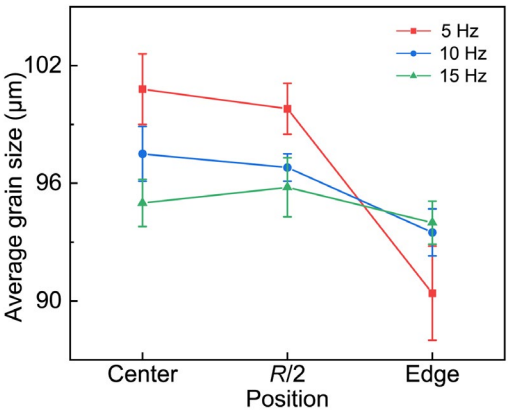


Fig. 16: Statistical results of average grain size at different frequencies with an input current of 100 A

parameters model at different stirring times with an input frequency of 15 Hz and an input current of 100 A is shown in Fig. 17. As the stirring time increases, the overall temperature of the melt continuously decreases and the temperature difference between the center and the outer wall of the melt gradually increases, thereby expanding the range of low-temperature ranges. Meanwhile, the temperature distribution in the upper part of the melt also shows a bending trend over time.

Figure 18 shows the temperature distribution of dynamic thermophysical parameters model at different stirring times with an input frequency of 15 Hz and an input current of 100 A. It can be seen from Fig. 18 that as time increases, due to electromagnetic stirring, the upper part of the melt fully exchanges heat with ambient air, resulting in a gradual downward expansion of the low-temperature region. At the same time, the low-temperature region in the lower part of the melt gradually expands from bottom to top, and the overall cross-sectional temperature distribution of the melt is relatively uniform.

Figure 19 shows the temperature variation with time at the melt center with a height of 30 mm. The temperature at the monitoring points of the constant parameter model shows a significant linear decrease, while the temperature at the monitoring points of the dynamic parameter model shows a relatively small and fluctuant decrease. Although the measuring point with the lowest velocity in the middle and lower part of the melt was selected, the thermocouple probe at the monitoring point is still affected by the fluctuations of the melt, resulting in fluctuations in the measurement result curve. After fitting the fluctuating temperature measurements, it is found that the calculated curve of the dynamic thermophysical parameter model is closer to the curve fitted by the experimental measurements.

The particle tracking method for key points can further demonstrate the rationality of velocity and temperature field distributions in the dynamic parameter model. Figure 20 illustrates the specified particle motion with an input frequency of 15 Hz and an input current of 100 A. It can be seen from the legends of the first and fifth seconds that the Point-1 in

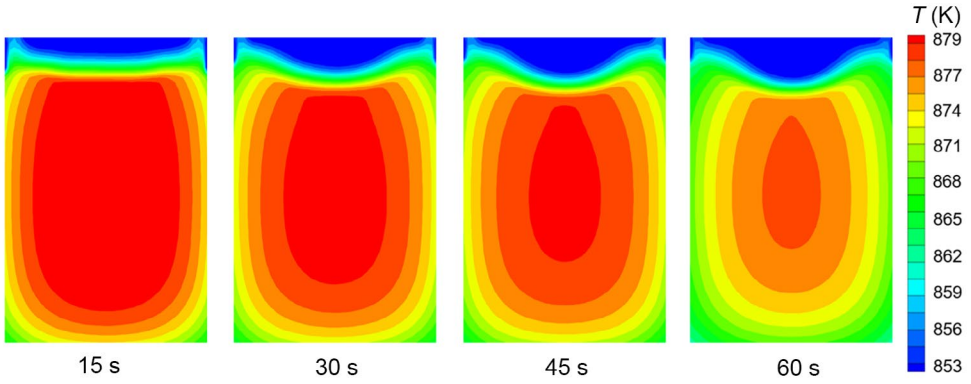


Fig. 17: Temperature distribution in constant parameters model at different times with an input frequency of 15 Hz and an input current of 100 A

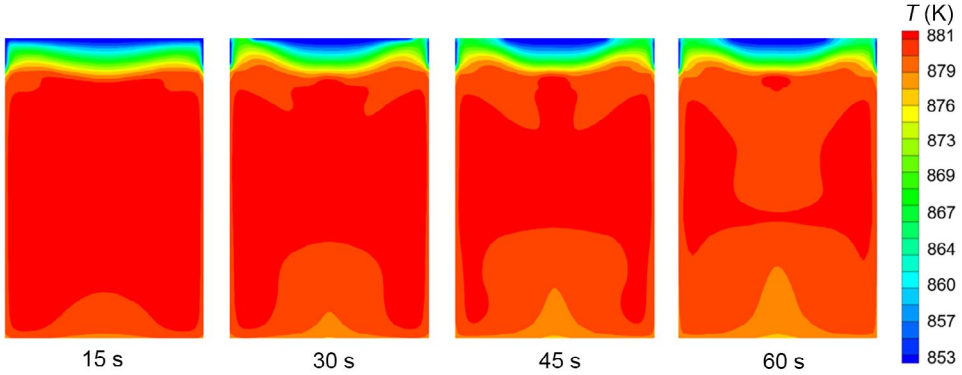


Fig. 18: Temperature distribution in dynamic parameters model at different times with an input frequency of 15 Hz and an input current of 100 A

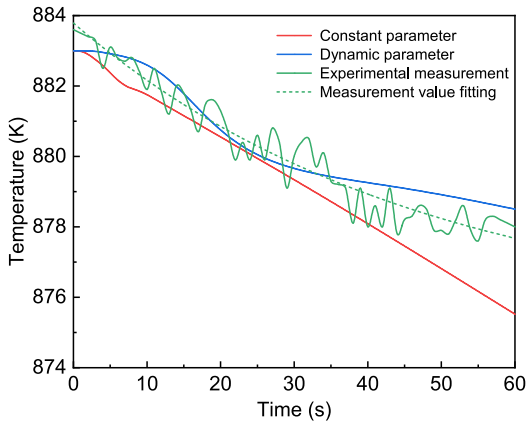


Fig. 19: Change in temperature with time along radial direction with a height of 30 mm

the dynamic parameter model moves from the outer circle to the inner circle on the plane and gradually moves towards the bottom. Meanwhile, Point-2 moves to the bottom, then gradually moves from the inner circle to the outer circle, and rises helically along the near-wall region of the melt until it reaches the mid-height region of the melt. After that, the particles move in a spiral downward manner from near the wall at the longitudinal middle of the melt to the center of the melt bottom and then undergo circulation. The particles circulate in the middle and lower part of the melt and forming a vortex, so that heat is transferred from the middle part of the melt to the walls, which causes the temperature image of the dynamic parametric model to appear as a conical region of lower temperature in the middle and lower parts of the melt. However, the points in the constant parameter model move almost in a circular motion in the plane over time, and the center melt is not carried to the wall by vortices when the velocity field is stable, which results in a temperature distribution trend that is the similar as the heat transfer from solidification in the absence of electromagnetic stirring. This also explains why the application of a magnetic field has almost no effect on the heat dissipation trend when using a constant parameter model.

4 Conclusions

In this study, the influence of physical parameters related to thermal changes on the semi-solid melt model was studied by constructing a three-dimensional multiphase flow model with thermal coupling of magnetic fluids. Based on multi-physics field simulations and combined with verification experiments, the differences between constant and dynamic thermophysical parameters in the electromagnetic stirring simulation process were analyzed. The main conclusions are as follows:

(1) The thickness of the gas-liquid mixing zone for the constant parameter model is almost independent of time and frequency, and the magnitude of the liquid level fluctuations progressively increases with time and frequency. However, the gas-liquid mixing zone exhibits inconsistency with the constant parameter model due to the influence of dynamic thermophysical parameters. The amplitude

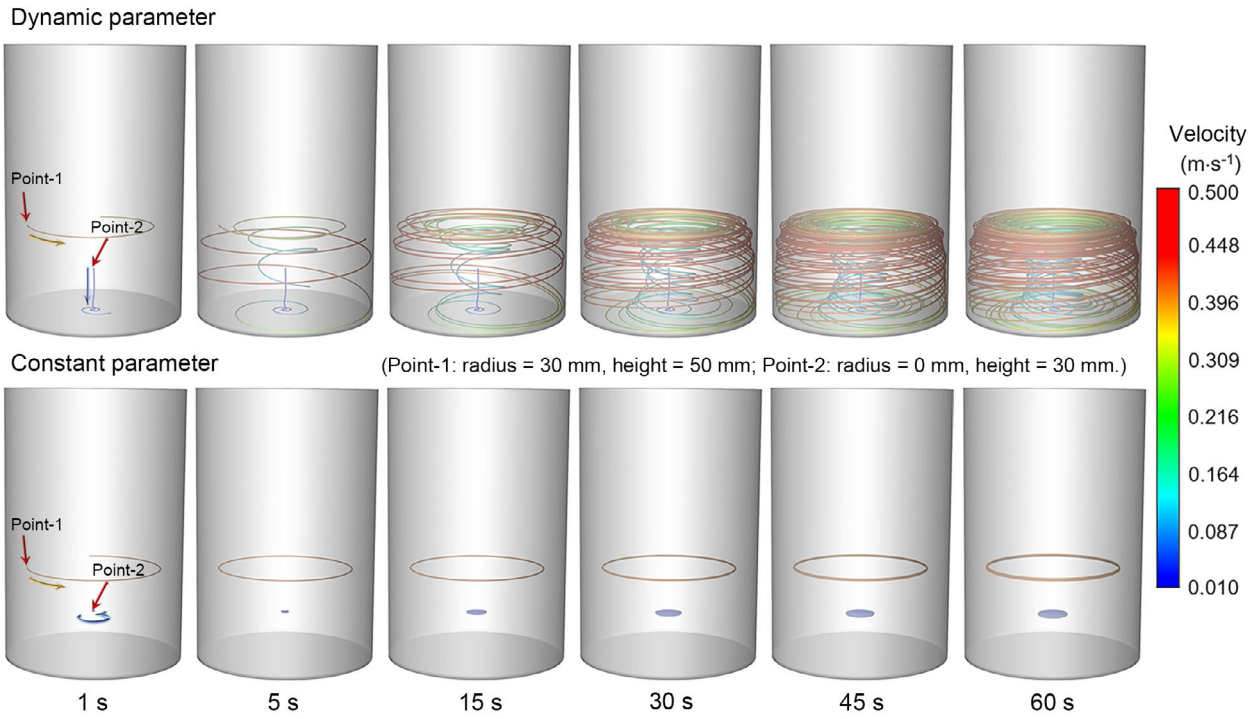


Fig. 20: Particles motion at different times with an input frequency of 15 Hz and an input current of 100 A

of liquid level fluctuations decreases with time, and the gas-liquid mixing zone thickness gradually expands to a certain extent. It is consistent with the actual situation, since the viscosity gradually increases and the degree of liquid level fluctuation gradually decreases over time due to the decrease in temperature.

(2) The velocity band of the constant parameter model shows a vertical distribution. The velocity distribution of models with dynamic thermophysical parameters differs from models with constant parameters in that high-velocity zones have a crescent-symmetric distribution in the vertical cross section. At the velocity monitoring point, the velocity shows a fluctuating and decreasing trend over time. Obviously, simulation models using dynamic thermophysical parameters are relatively more realistic.

(3) The presence of a magnetic field has little effect on the trend of the temperature distribution when using a constant parameters model. When using a dynamic thermophysical parameters model and conducting electromagnetic stirring on the melt, the temperature distribution trend is significantly different from that without electromagnetic stirring. The same conclusion is obtained by analyzing the metallographic diagram. The temperature of the melt gradually decreases over time at both the top and bottom of the melt, and the heat dissipation trend is visualized by tracking particle motion. In addition, when setting temperature monitoring point for observation, it is found that the calculation curve of the dynamic thermophysical parameters model is closer to the curve fitted by experimental measured values.

In summary, numerical models established using physical parameters related to dynamic thermal changes can more accurately predict the distribution trend of physical fields.

Acknowledgment

This work was supported by the Fundamental Research Foundation for Universities of Heilongjiang Province (Grant No. 2022-KYYWF-0127).

Conflict of interest

The authors declare that they have no known competing financial interests or personal relationships that could have appeared to influence the work reported in this paper.

References

[1] Chang Z, Su N, Wu Y, et al. Semisolid rheoforming of magnesium alloys: A review. Materials & Design, 2020, 195: 108990. https://doi.org/10.1016/j.matdes.2020.108990.

[2] Khanouki M T A. Mechanical properties and microstructural evolution of rheocast A356 semi-solid slurry prepared by annular electromagnetic stirring. China Foundry, 2023, 20(4): 315–328. https://doi.org/10.1007/s41230-023-3041-2.

[3] Liu G, Ren Y, Ma W, et al. Recent advances and future trend of aluminum alloy melt purification: A review. Journal of Materials Research and Technology, 2024, 28: 4647–4662. https://doi.org/10.1016/j.jmrt.2024.01.024.

[4] Sun J, Le Q, Fu L, et al. Gas entrainment behavior of aluminum alloy engine crankcases during the low-pressure-die-casting process. Journal of Materials Processing Technology, 2019, 266: 274–282. https://doi.org/10.1016/j.jmatprotec.2018.11.016.

[5] Balasubramani N, Venezuela J, Yang N, et al. An overview and critical assessment of the mechanisms of microstructural refinement during ultrasonic solidification of metals. Ultrasonics Sonochemistry, 2022, 89: 106151. https://doi.org/10.1016/j.ultsonch.2022.106151.

[6] Liu Y, Meng S, Gao M, et al. Enhanced comprehensive performance via alloying and rheo-diecasting in a semi-solid Al-Si-Fe-Mg-Cu-Sr alloy. Journal of Materials Research and Technology, 2023, 25: 420–439. https://doi.org/10.1016/j.jmrt.2023.05.222.
[7] Karakulak E. A review: Past, present and future of grain refining of magnesium castings. Journal of Magnesium and Alloys, 2019, 7(3): 355–369. https://doi.org/10.1016/j.jma.2019.05.001.
[8] Erbas K C. Determination of position-dependent solid fraction by a new cooling curve analysis method: Semi-Newtonian Fourier thermal analysis. International Communications in Heat and Mass Transfer, 2021, 126: 105353. https://doi.org/10.1016/j.icheatmasstransfer.2021.105353.
[9] Czerwinski F. Thermomechanical processing of metal feedstock for semisolid forming: A review. Metallurgical and Materials Transactions: B, 2018, 49: 3220–3257. https://doi.org/10.1007/s11663-018-1387-4.
[10] Hu M, Yang L, Yi W, et al. Entrainment defects in semi-solid A356 aluminum alloy treated by ICTE process. Journal of Alloys and Compounds, 2023, 963: 171237. https://doi.org/10.1016/j.jallcom.2023.171237.
[11] Yang Y, Liu X, and Wang S. Thermal characteristics of induction heating with stepped diameter mold during two-phase zone continuous casting high-strength aluminum alloys. International Journal of Heat and Mass Transfer, 2020, 152: 119479. https://doi.org/10.1016/j.ijheatmasstransfer.2020.119479.
[12] Wu G, Wang C, Sun M, et al. Recent developments and applications on high-performance cast magnesium rare-earth alloys. Journal of Magnesium and Alloys, 2021, 9(1): 1–20. https://doi.org/10.1016/j.jma.2020.06.021.
[13] Yang Z and He J. Numerical investigation on fluid transport phenomena in electron beam welding of aluminum alloy: Effect of the focus position and incident beam angle on the molten pool behavior. International Journal of Thermal Sciences, 2021, 164: 106914. https://doi.org/10.1016/j.ijthermalsci.2021.106914.
[14] Liang Y, Xu Y, Guan J, et al. Experimental study on fouling inhibition characteristics of a variable frequency electromagnetic field on the $CaCO_3$ fouling of a heat transfer surface. International Journal of Heat and Mass Transfer, 2022, 190: 122756. https://doi.org/10.1016/j.ijheatmasstransfer.2022.122756.
[15] Balasubramani N, Venezuela J, StJohn D, et al. A review of the origin of equiaxed grains during solidification under mechanical stirring, vibration, electromagnetic, electric-current, and ultrasonic treatments. Journal of Materials Science & Technology, 2023, 144: 243–265. https://doi.org/10.1016/j.jmst.2022.09.067.
[16] Aryal P, Sikstrom F, Nilsson H, et al. Comparative study of the main electromagnetic models applied to melt pool prediction with gas metal arc: Effect on flow, ripples from drop impact, and geometry. International Journal of Heat and Mass Transfer, 2022, 194: 123068. https://doi.org/10.1016/j.ijheatmasstransfer.2022.123068.
[17] Yang C, Yang F, Meng X, et al. Phase-field simulation of the dendrite growth in aluminum alloy AA5754 during alternating current electromagnetic stirring laser beam welding. International Journal of Heat and Mass Transfer, 2024, 218: 124754. https://doi.org/10.1016/j.ijheatmasstransfer.2023.124754.
[18] Liu W, Li T, Wang T, et al. Analysis of the influence of roll size change on electromagnetic heat conversion capacity and roll profile control characteristics in the RPECT. International Journal of Heat and Mass Transfer, 2022, 189: 122686. https://doi.org/10.1016/j.ijheatmasstransfer.2022.122686.
[19] Xu L, Karcher C, and Wang E. Numerical simulation of melt flow, heat transfer and solidification in CSP continuous casting mold with vertical-combined electromagnetic braking. Metallurgical and Materials Transactions: B, 2023, 54(4): 1646–1664. https://doi.org/10.1007/s11663-023-02784-7.
[20] Aryal P and Choquet I. Melt pool electromagnetic force model extended to account for free surface deformation – Application to gas metal arc. International Journal of Heat and Mass Transfer, 2024, 221: 124987. https://doi.org/10.1016/j.ijheatmasstransfer.2023.124987.
[21] Yao C, Wang M, Zhang M, et al. Effects of mold electromagnetic stirring on heat transfer, species transfer and solidification characteristics of continuous casting round billet. Journal of Materials Research and Technology, 2022, 19: 1766–1776. https://doi.org/10.1016/j.jmrt.2022.05.167.
[22] Maurya A, Kumar R, and Jha P K. Simulation of electromagnetic field and its effect during electromagnetic stirring in continuous casting mold. Journal of Manufacturing Processes, 2020, 60: 596–607. https://doi.org/10.1016/j.jmapro.2020.11.003.
[23] Maurya A and Jha P K. Influence of electromagnetic stirrer position on fluid flow and solidification in continuous casting mold. Applied Mathematical Modelling, 2017, 48: 736–748. https://doi.org/10.1016/j.apm.2017.02.029.
[24] Kang K, Jiang S, Li D, et al. Effect of electric pulse and rotating magnetic field on solidification microstructure and properties of Al-Zn-Mg-Cu alloy. Materials Characterization, 2023, 200: 112906. https://doi.org/10.1016/j.matchar.2023.112906.
[25] Guan R, Ji C, and Zhu M. Modeling the effect of combined electromagnetic stirring modes on macrosegregation in continuous casting blooms. Metallurgical and Materials Transactions: B, 2020, 51: 1137–1153. https://doi.org/10.1007/s11663-020-01827-7.
[26] Huo Y K, Zhao L H, An H H, et al. Model prediction of the effect of in-mold electromagnetic stirring on negative segregation under bloom surface. International Journal of Minerals, Metallurgy and Materials, 2020, 27: 319–327. https://doi.org/10.1007/s12613-019-1906-6.
[27] Wang Y, Zhao S, and Guo Y. Numerical simulation and experimental investigation of the preparation of aluminium alloy 2A50 semi-solid billet by electromagnetic stirring. Materials, 2020, 13(23): 5470. https://doi.org/10.3390/ma13235470.
[28] Luo H, Zhang X, Wang Y, et al. Multi-physics coupled numerical simulation study to optimize process parameters for electromagnetic stirring of semi-solid A356 aluminum alloy under the influence of skin effect. International Communications in Heat and Mass Transfer, 2024, 157: 107834. https://doi.org/10.1016/j.icheatmasstransfer.2024.107834.
[29] Rusanov B A, Sidorov V E, Moroz A I, et al. Density and electrical resistivity of Al-Ni-Co-Sm (Tb) alloys. Technical Physics Letters, 2021, 47(10): 770–772. https://doi.org/10.21883/PJTF.2021.15.51233.18839.
[30] Fang L, Zhang S F, Xiao F, et al. Measurement and analysis of liquid density of Ni-Al binary alloys. Journal of Alloys and Compounds, 2010, 493(1–2): 465–470. https://doi.org/10.1016/j.jallcom.2009.12.128.
[31] Magnusson T and Arnberg L. Density and solidification shrinkage of hypoeutectic aluminum-silicon alloys. Metallurgical and Materials Transactions: A, 2001, 32: 2605–2613. https://doi.org/10.1007/s11661-001-0050-9.
[32] Assael M J, Kakosimos K, Banish R M, et al. Reference data for the density and viscosity of liquid aluminum and liquid iron. Journal of physical and Chemical Reference Data, 2006, 35(1): 285–300. https://doi.org/10.1063/1.2149380.
[33] Poirier D R. Density, viscosity, and diffusion coefficients in hypoeutectic Al-Si liquid alloys: An assessment of available data. Metallurgical and Materials Transactions: B, 2014, 45: 1345–1354. https://doi.org/10.1007/s11663-014-0037-8.

[34] Assael M J, Mihailidou E K, Brillo J, et al. Reference correlation for the density and viscosity of eutectic liquid alloys Al+Si, Pb+Bi, and Pb+Sn. Journal of Physical and Chemical Reference Data, 2012, 41(3): 033103. https://doi.org/10.1063/1.4750035.

[35] Beltyukov A, Ladyanov V, and Sterkhova I. Effect of small nickel additions on viscosity of liquid aluminum. Journal of Molecular Liquids, 2019, 296: 111764. https://doi.org/10.1016/j.molliq.2019.111764.

[36] Garoosi F and Hooman K. Numerical simulation of multiphase flows using an enhanced volume-of-fluid (VOF) method. International Journal of Mechanical Sciences, 2022, 215: 106956. https://doi.org/10.1016/j.ijmecsci.2021.106956.

[37] Bures L and Sato Y. Direct numerical simulation of evaporation and condensation with the geometric VOF method and a sharp-interface phase-change model. International Journal of Heat and Mass Transfer, 2021, 173: 121233. https://doi.org/10.1016/j.ijheatmasstransfer.2021.121233.

[38] Sklyarchuk V, Plevachuk Y, Yakymovych A, et al. Structure sensitive properties of liquid Al-Si alloys. International Journal of Thermophysics, 2009, 30: 1400–1410. https://doi.org/10.1007/s10765-009-0585-3.

[39] Stacy S C, Zhang X, Pantoya M, et al. The effects of density on thermal conductivity and absorption coefficient for consolidated aluminum nanoparticles. International Journal of Heat and Mass Transfer, 2014, 73: 595–599. https://doi.org/10.1016/j.ijheatmasstransfer.2014.02.050.

[40] Koizumi H, Koizumi T, and Kosugi T. Determination of the pre-exponential factor and the activation energy for the low-temperature dislocation relaxation in aluminum. Journal of Alloys and Compounds, 2000, 310(1): 107–110. https://doi.org/10.1016/S0925-8388(00)00926-9.

[41] Overfelt A R, Bakhtiyarov I S, and Taylor E R. Thermophysical properties of A201, A319, and A356 aluminium casting alloys. High Temperatures-High Pressures, 2002, 34(4): 401–409. https://doi.org/10.1068/htjr052.

[42] Jafari M, Zebarjad S, and Kolahan F. Simulation of thixoformability of A356 aluminum alloy using finite volume method. Materials Science & Engineering: A, 2006, 454–455: 558–563. https://doi.org/10.1016/j.msea.2006.11.124.